TU Delft

Delft University of Technology

Enhanced phishing detection using multimodal data

Bustio-Martínez, Lázaro; Herrera-Semenets, Vitali; González-Ordiano, Jorge Ángel; Pérez-Guadarramas, Yamel; Zúñiga-Morales, Luis; Montoya-Godínez , Daniela ; Álvarez-Carmona, Miguel Ángel ; van den Berg, Jan

DOI
10.1016/j.knosys.2025.115105

Publication date
2025

Document Version
Final published version

Published in
Knowledge-Based Systems

Citation (APA)
Bustio-Martínez, L., Herrera-Semenets, V., González-Ordiano, J. Á., Pérez-Guadarramas, Y., Zúñiga-Morales, L., Montoya-Godínez , D., Álvarez-Carmona, M. Á., & van den Berg, J. (2025). Enhanced phishing detection using multimodal data. *Knowledge-Based Systems*, *334*, Article 115105. https://doi.org/10.1016/j.knosys.2025.115105

Important note
To cite this publication, please use the final published version (if applicable).
Please check the document version above.

Copyright
Other than for strictly personal use, it is not permitted to download, forward or distribute the text or part of it, without the consent of the author(s) and/or copyright holder(s), unless the work is under an open content license such as Creative Commons.

Takedown policy
Please contact us and provide details if you believe this document breaches copyrights.
We will remove access to the work immediately and investigate your claim.

This work is downloaded from Delft University of Technology.
For technical reasons the number of authors shown on this cover page is limited to a maximum of 10.

Theoretical and Applied Fracture Mechanics 142 (2026) 105400

Contents lists available at ScienceDirect

Theoretical and Applied Fracture Mechanics

journal homepage: www.elsevier.com/locate/tafmec

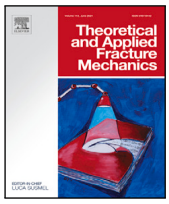

Mode I fracture toughness of co-bonded metal–composite joints with additively manufactured titanium: Influence of printing parameters

Michele Gulino [a,*], Rosemere de Araujo Alves Lima [b], Fabrizio Moroni [a], Francesco Musiari [a], Alessandro Pirondi [a], Sofia Teixeira de Freitas [b,c]

[a] Department of Engineering for Industrial Systems and Technologies, University of Parma, Parco Area delle Scienze 181/A, Parma, Italy
[b] IDMEC, Instituto Superior Técnico, Universidade de Lisboa, Av. Rovisco Pais 1, Lisboa, Portugal
[c] Department of Aerospace Engineering, Delft University of Technology, Kluyverweg 1, Delft, The Netherlands

ARTICLE INFO

Keywords:
Mode I fracture toughness
Carbon Fiber Reinforced Polymers (CFRP)
Titanium Ti6Al4V
Co-bonding
Double Cantilever Beam (DCB) test
Laser Powder Bed Fusion (LPBF)

ABSTRACT

The strength of adhesive joints is influenced by the surface of the adherends, which is often treated before bonding to prevent interfacial (adhesive) failure. Laser Powder Bed Fusion (LPBF) offers promising potential for bonding without time-consuming surface treatments, since LPBF parts have an inherently rough surface, which is usually associated with good adhesion strength. Here we study the effect of the printing parameters on the mode I fracture toughness of co-bonded joints between untreated LPBF Ti6Al4V and Carbon Fiber Reinforced Polymer (CFRP) substrates. A factorial Design of Experiment (DoE) was set varying the laser scan speed and the build angle of the Ti6Al4V substrates, which were co-bonded with a CFRP woven laminate to form Double Cantilever Beam (DCB) joints. The results showed that increasing the scan speed from 500 mm/s to 2000 mm/s led to higher titanium surface roughness (+125% on average). On the other hand, the mode I fracture toughness was mainly affected by the build angle: the joints with vertically printed (90° with respect to the build platform) titanium adherends exhibited, on average, a 200% increase in toughness compared to the samples with titanium printed at an angle. This behavior was due to the higher number of partially melted particles on the surface of the vertical joints. A particle counting method was introduced to quantify the partially fused particles and their correlation with the mode I fracture toughness was demonstrated. Moreover, to the authors' knowledge, for the first time an original approach was proposed to assess their interlocking contribution to joint toughness.

1. Introduction

Adhesive bonding is a highly effective technique for joining Fiber Reinforced Polymers (FRPs) and metals, which is crucial for the production of lightweight, multi-material structures. It offers significant weight savings, especially for long bond lines where multiple rivets or bolts would otherwise be required [1,2]. Additionally, it provides a larger load-bearing area and eliminates the need to drill into composite adherends, reducing stress concentrations and minimizing the risk of delamination [3].

Despite its many advantages, adhesive joints are typically prone to brittle failure modes, which hinder their application in critical components. Consequently, they have yet to be certified for primary aircraft structures, where hybrid adhesive-riveted joints are often preferred as a more reliable alternative, given their structural redundancy [4,5].

To this end, research has focused on several toughening methods. For instance, introducing structured or non-flat interfaces has been shown to redistribute peel and shear stresses along the bondline, leading to strength improvements of up to 40% [6,7]. Crack-arresting features and carrier mats embedded in the adhesive can also increase the macroscopic fracture toughness of the joint by up to 50% [8,9]. Furthermore, through-the-thickness reinforcements such as z-pins or 3D printed micro-anchors have demonstrated substantial gains performance over unreinforced joints [10–14], with shear strength, tensile strength and fracture toughness reaching up to 6.5× [13], 10× [15] and 19× [16], respectively. Another strategy is grading of the adhesive properties across the bondline, which reduces peel stresses and enhances joint strength by up to 45% [17]. However, the most widely

* Corresponding author.
E-mail address: michele.gulino@unipr.it (M. Gulino).

https://doi.org/10.1016/j.tafmec.2025.105400
Received 30 September 2025; Received in revised form 11 December 2025; Accepted 11 December 2025
0167-8442/© 2025 The Authors. Published by Elsevier Ltd. This is an open access article under the CC BY license (http://creativecommons.org/licenses/by/4.0/).

studied toughening method relies on surface pretreatments to increase wettability and adhesion, promoting cohesive failure and resulting in significant strength gains [18–20].

These treatments typically increase surface roughness, which is often linked to strong adhesion. However, these processes are time-consuming, difficult to perform consistently, and may leave defects undetectable with Non-Destructive Inspection (NDI) techniques, which can lead to unexpected joint failure.

Additive Manufacturing (AM), particularly Laser Powder Bed Fusion (LPBF), inherently produces parts with high surface roughness, which enables mechanical interlocking, as seen in surfaces treated with sandblasting or anodic oxidation [1,21], and making it a promising alternative for adhesive bonding without surface treatments [22–25], with researchers reporting roughness values over 20 μm [23]. Furthermore, LPBF allows for the creation of structured interfaces with virtually unlimited geometric freedom, such as lattice structures (with limits only regarding the maximum overhead angle of about 45°) [26] and its reliability is being improved through in-situ process monitoring and control strategies, such as melt pool data collection via co-axial imaging to track the pool geometry and temperature distribution during fabrication [27]. Therefore, as-printed LPBF substrates offer a potential cost-efficient solution for adhesive bonding in metal–composite joints.

The adhesion strength of the as-printed LPBF surface in metal–metal bonded joints has been studied only in a few different works by Ertürk [28], Koch [29], Ardila-Rodríguez [30], and Naat [31] where joints with untreated LPBF printed adherends have been compared to similar joints but with treated adherends. The results showed that the as-printed LPBF surface offered a comparable [30] or even higher [28,31], adhesion strength than that of surface-treated joints. Only two works on the topic of LPBF metal–CFRP joints were found in literature [32,33]. In the investigation of Nguyen [32], LPBF titanium was either co-cured with CFRP or bonded with another LPBF titanium adherend, without undergoing surface treatment, to form DCB joints. The tested joints exhibited mostly cohesive failure and crack deflection in the composite, showing the potential of the untreated LPBF surface morphology. In the work of Fielden-Stewart et al. [33], it was shown that the mixed-mode fracture toughness of LPBF aluminum–CFRP secondary bonded joints printed with several build angles was higher for untreated joints compared to mechanically abraded joints, regardless of the build angle.

Despite the growing interest in using LPBF metal substrates in bonded joints, the literature reveals several gaps in understanding how their surface morphology affects adhesion performance. While studies on metal–metal bonded joints with untreated LPBF adherends have demonstrated comparable or superior adhesion strength to treated surfaces [28–31], these works did not use fracture toughness as a metric for adhesion strength, which provides deeper insights into failure mechanisms [34]. Moreover, limited attention has been given to the interaction between untreated LPBF adherends and composite materials. Existing research on LPBF metal–composite joints has primarily focused on through-the-thickness reinforcements, such as pins [16] or lattice structures [14,15], with little attention to the intrinsic surface characteristics of untreated LPBF substrates. Notably, the only two studies addressing LPBF metal–CFRPP joints without such reinforcements (from Nguyen [32] and Fielden-Stewart [33]) demonstrate the potential for mechanical interlocking and higher fracture toughness in untreated LPBF substrates. However, these studies do not assess the role of surface treatments such as sandblasting nor the impact of LPBF printing parameters on the adhesion performance of co-bonded joints. This highlights the need for a comprehensive evaluation of untreated LPBF surfaces in co-bonded joints, particularly regarding their suitability for high-performance applications.

In addition, while prior studies have qualitatively discussed the potential role of partially fused particles in promoting mechanical interlocking at the interface, a quantitative investigation has so far been lacking.

Building on our previous findings on the potential and limitations of bonding LPBF substrates without surface treatments [35,36], this study aims to address this gap by investigating how variations in printing parameters affect the mode I fracture toughness of titanium–CFRP co-bonded DCB joints, and quantifies the contribution of partially fused surface particles to mechanical interlocking. It is hypothesized that (i) variations in LPBF process parameters have a significant effect on the mode I fracture toughness of co-bonded joints, and (ii) the interfacial strength of these joints cannot be reliably predicted by conventional roughness metrics but rather by alternative surface descriptors capturing surface quality and morphology. The experimental campaign involves co-bonding of Ti6Al4V–CFRP DCB joints, detailed surface characterization, and mode I fracture testing.

2. Materials and methods

2.1. Design of experiment and manufacturing of the LPBF adherends

The titanium adherends (Fig. 1), provided by 3T-Additive Manufacturing (Newbury, United Kingdom), were printed with an M290 SLM machine (EOS Gmbh, Krailling, Germany). The titanium powder had an average particle diameter of 37.3 μm and a nominal particle size range between 20 μm and 63 μm, achieved via sieving. All the adherends were printed with 60 μm layer thickness, 190 W laser power and 80 μm spot size. As shown in Fig. 1, the adherends have 6 mm thickness, 130 mm length and 25 mm width, and were printed with a loading block, which was then drilled to allow the positioning of the pin for the mode I loading in the testing machine.

A full factorial DoE with 2 printing parameters varied on 2 levels (2^2 factorial) with a center point was used to assess their influence on the fracture toughness of the co-bonded joints. Specifically, the build angle and the laser scan speed were the parameters of choice after a preliminary study (please refer to the Appendix of this paper), with the former varying between 90° and 130° (between the bonding surface and the build platform) and the latter between 500 mm/s and 2000 mm/s; the center point's parameters values were 110° and 1250 mm/s. Three specimens were tested for each design point, for a total of 15 specimens. The samples were named after the level of the printing parameters: the first two/three digits correspond to the build angle, while the last four to the scan speed (e.g. 90-0500 = 90° build angle and 500 mm/s scan speed). The experiment matrix with the naming of the samples is shown in Fig. 2. It must be noted that thermal residual stresses intrinsically present in LPBF titanium adherends were previously characterized and found not to influence the mode-I fracture toughness of untreated metal–composite joints with LPBF titanium adherends [36]. For this reason, no stress-relief heat treatment was applied to the substrates in this study.

2.2. Optical profilometry and water contact angle measurements

The surface morphology of the titanium adherends was inspected with a non-contact optical profilometer (Taylor-Hobson, Leicester, UK) before the co-bonding. Three scans of 1.71×1.71 mm^2 area were taken across the bonding surface of each adherend, one close to the load application line, one in the central region of the faying surface, and one at the rear end of the adherend.

The wettability of the titanium substrates was qualitatively evaluated with water contact angle measurements, using an optical contact angle measurement system from DataPhysics Instruments GmbH (Filderstadt, Germany).

Water droplets of 10 μl were deposited on each specimen and the image was acquired after 10 s. A total of 4 droplets for each adherend was inspected across the adherend's surface to give statistical significance to the test.

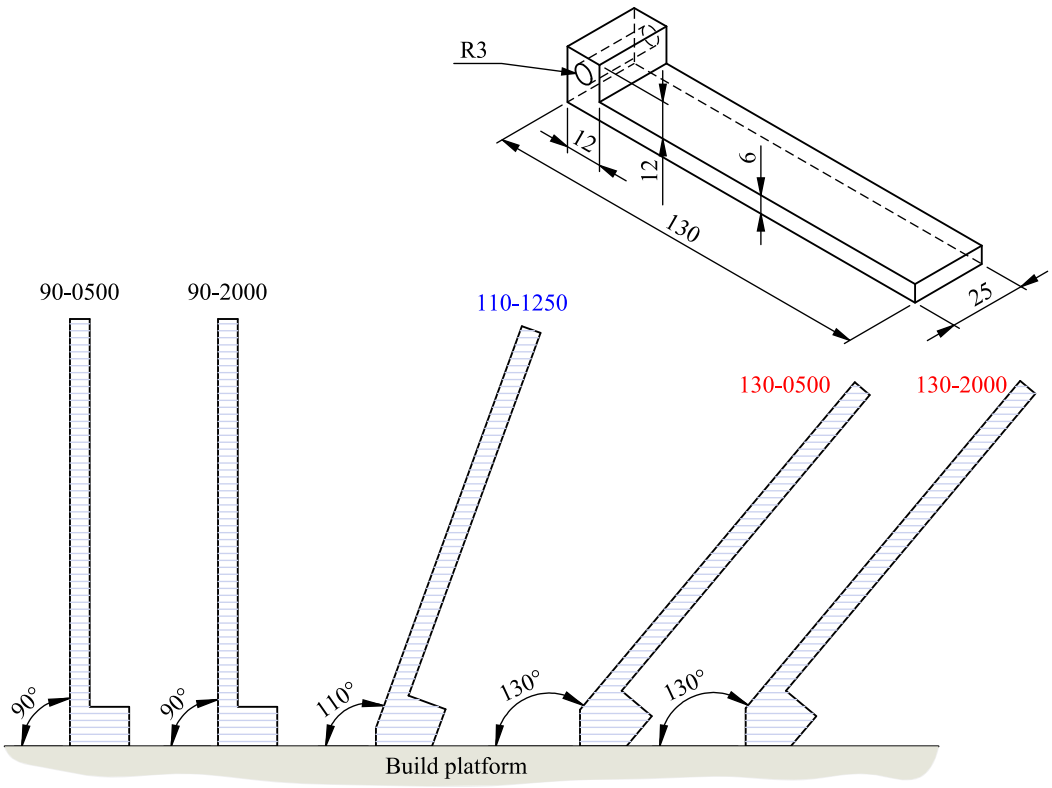

Fig. 1. Dimensions of the titanium substrates (in millimeters), and schematic representation of the build platform showing the five printing configurations. The first digits of the nomenclature represent the build angle, the last four digits represent the scan speed. Each configuration includes three repetitions, for a total of fifteen adherends.

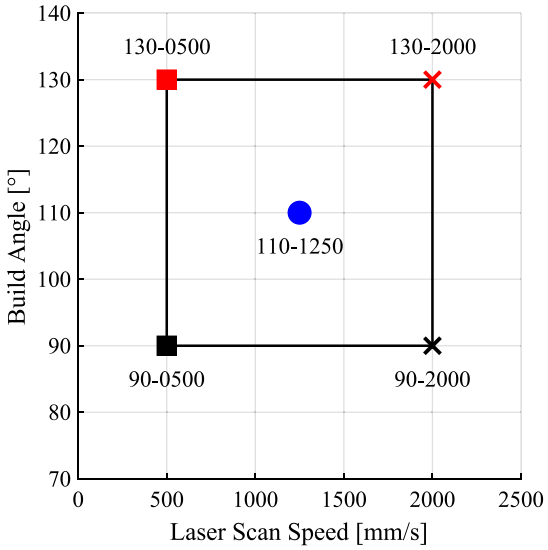

Fig. 2. Visual representation of the experiment matrix with the name of the samples.

2.3. Manufacturing of the co-bonded DCB joints and materials properties

The co-bonding was performed by Bercella Srl (Varano de' Melegari, Italy) with vacuum bag and autoclave curing for 2 h at 130 °C and 6 bar of external pressure. GG630T – DT120 woven CFRP prepregs with $[0\text{-}90]_{13}$ stacking sequence were used to manufacture the composite adherends, followed by 15 strips of Hexbond ST 1035 (Hexcel, Stamford, USA) epoxy film adhesive supported with a polyester carrier mat (300 g/m^2 areal density). The titanium adherends were cleaned in an ultrasonic acetone bath for 10 min and then placed on the adhesive. Teflon spacers (15 mm wide and same length and thickness as the titanium adherends) were used between the adherends to allow the cut of the laminate to separate each sample. A Teflon strip placed at 15 mm from the load line of the specimens was used as initial defect.

After the co-bonding, the samples were cut and machined to dimension, and a loading block was adhesively bonded to the CFRP adherends (Fig. 3, Table 1). The adhesive thickness h_a was assumed to be equal to that of the carrier mat (0.1 mm, Table 2), as the adhesive layer was not clearly visible from the side of the samples. The thickness of the CFRP adherends h_{cfrp} was determined by subtracting the titanium adherend thickness h_{ti} from the total joint thickness h_{tot}.

The number of CFRP prepreg plies was selected to achieve the target thickness of 8.23 mm, required for pure mode I loading, according to the longitudinal strain based method proposed by Wang et al. [37]. However, the actual thickness of the CFRP substrates slightly deviated from the target value, introducing a small percentage of mixed-mode loading.

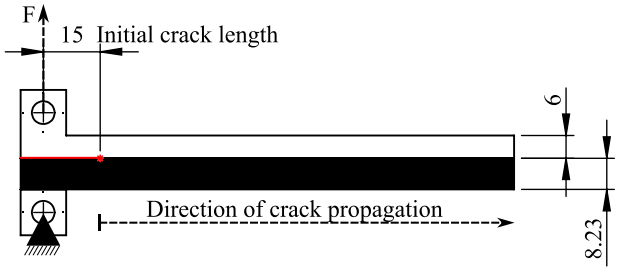

Fig. 3. Geometry of the DCB co-bonded joints, with nominal thicknesses of the adherends and nominal initial crack length. All dimensions in millimeters.

Table 1
Dimensions and mixed mode ratio of the DCB samples.

3 repetitions per batch	b [mm]	h_{tot} [mm]	h_{ti} [mm]	h_{cfrp} [mm]	h_a [mm]	$G_{II\%}$ [%]
90-0500	25.02 ± 0.06	14.68 ± 0.05	6.21 ± 0.01	8.38 ± 0.05		5.42
90-2000	24.90 ± 0.04	14.57 ± 0.07	6.19 ± 0.02	8.29 ± 0.07		4.60
110-1250	24.91 ± 0.02	14.45 ± 0.07	6.22 ± 0.04	8.13 ± 0.06	0.1	6.28
130-0500	24.88 ± 0.03	14.14 ± 0.08	6.28 ± 0.03	7.76 ± 0.09		6.50
130-2000	24.98 ± 0.03	14.26 ± 0.11	6.30 ± 0.06	7.86 ± 0.09		6.30

Table 2
Mechanical properties of the adherends.

Ti6Al4V		GG630T-DT120		Structil ST 1035	
E_{ti} [36]	G_{ti} [36]	E_{cfrp} [36]	G_{cfrp} [36]	Carrier thickness [36]	$G_{Ic-adhesive}$ [35]
[MPa]		[MPa]		[mm]	[kJ/m^2]
118 030	44 041	60 079	2556	0.1	1.18

This deviation is reflected in the mixed-mode ratios ($G_{II\%}$) shown in Table 1, which represent the percentage ratio of the mode II component of the energy release rate to the total energy release rate. These values were calculated using Finite Element (FE) Virtual Crack Closure Technique (VCCT) models of the joints, following the method proposed by Wang et al. [37]. Given the low percentage of mode II contribution (up to 6.5%), the results presented in the following sections are expected to closely approximate the pure mode I condition. For this reason, the mode II percentage will be disregarded in the subsequent sections of the paper.

Further details regarding the selection of the 13 plies and the evaluation of the mixed-mode ratios can be found in the authors' previous work [36].

The main mechanical properties of the adherends were evaluated with tensile tests for the LPBF titanium and with three-point bending tests for the CFRP [35,36]. The mode I fracture toughness of the adhesive was evaluated with DCB tests on sandblasted aluminum adherends [35]. The thickness of the carrier mat was retrieved by dissolving the adhesive with acetone and measuring the polyester carrier with a digital micrometer gauge. The properties of the adherends and the adhesive are listed in Table 2.

2.4. Test setup and data reduction method

The DCB samples were tested using a Zwick-Roell electromechanical testing machine under displacement control, with a displacement rate of 2.5 mm/min — as suggested by the ASTM D5528 standard [38] — and a 10 kN load cell. The acquisition rate was set to 2 Hz. The Crack Mouth Opening Displacement (CMOD) was evaluated with 3-dimensional Digital Image Correlation (DIC) using the Vic 3D software by Correlated Solutions Inc (Irmo, USA) and 2 DIC cameras with 9 Megapixels sensors and 23 mm focal length. A speckle pattern was spray painted on the side of each joint, and two points on the loading line were drawn as reference for the virtual extensometer used to retrieve the CMOD. A rectangular region of interest was set around the reference points, and the subset and step sizes were 29 and 7 pixels, respectively (Fig. 4).

The DIC system was synchronized with the testing machine to retrieve the load associated to each DIC picture.

The Compliance Beam Based Method (CBBM, [39]) was used to calculate the mode I fracture toughness of the DCB joints. This method enables the evaluation of the crack length as a function of the compliance of the specimen. The test was carried out with periodic unloading and reloading, allowing the assessment of the compliance as the angular coefficient of the linear regression of the reloading phase, as shown in Fig. 5.

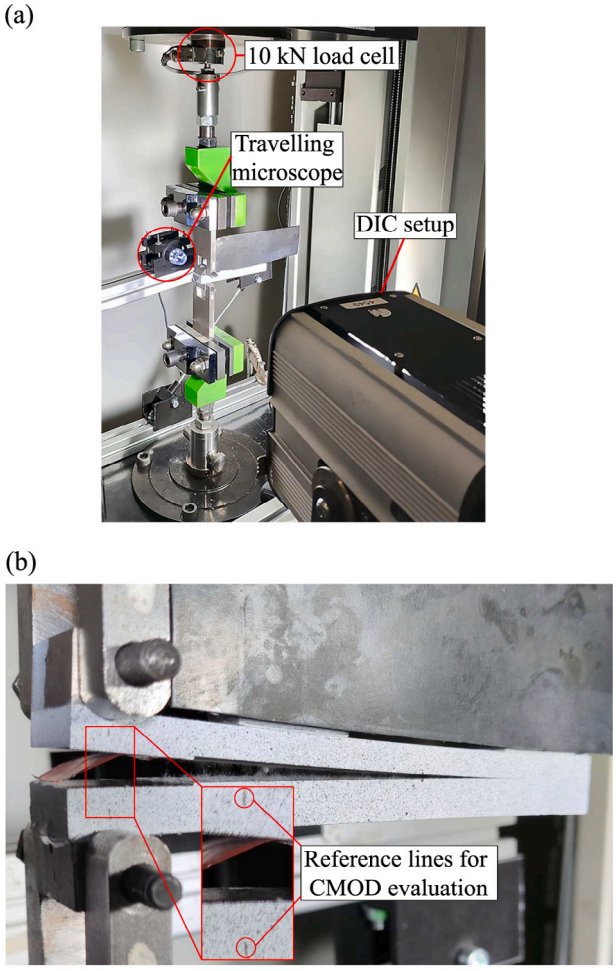

Fig. 4. (a) Test setup and (b) speckle pattern for the evaluation of the CMOD with DIC.

The CBBM models the DCB arms as Timoshenko beams (thus considering both bending and shear effects), and suggests the following formula relating the crack length a to the compliance C:

$$C^{as} = \left(\frac{CMOD}{F}\right)^{as} = \frac{a^3}{3}\left(\frac{12}{E_{ti}b_{ti}h_{ti}^3} + \frac{12}{E_{cfrp}bh_{cfrp}^3}\right) + \frac{6a}{5b}\left(\frac{1}{h_{ti}G_{ti}} + \frac{1}{h_{cfrp}G_{cfrp}}\right) \quad (1)$$

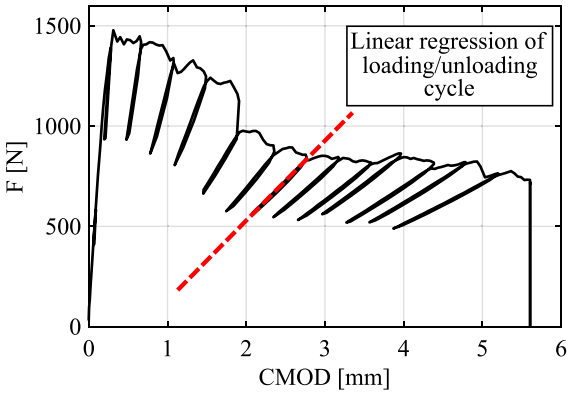

Fig. 5. Example of load–CMOD curve (sample 90-2000 1).

where F is the load, E and G are the adherends' flexural and out of plane shear moduli, h is the adherends' thickness, I is the second moment of area of the adherends' cross section, and b is the joint's width. The subscripts ti and $cfrp$ represent the titanium and the composite adherends, respectively. The crack length a for each unloading is retrieved solving Eq. (1). It is worth noting that, since the compliance of the joint is influenced by the Fracture Process Zone (FPZ) extending beyond the crack tip, the value evaluated with the CBBM should be regarded as the equivalent crack length "a_e" [39]. For simplicity, it will be referred to as "a". Knowing this value, the mode I fracture toughness can be calculated as:

$$G_{Ic}^{as} = \frac{F^2}{2b}\left[12a^2\left(\frac{1}{E_{ti}bh_{ti}^3}+\frac{1}{E_{cfrp}bh_{cfrp}^3}\right)+\frac{6a}{5b}\left(\frac{1}{G_{ti}h_{ti}}+\frac{1}{G_{cfrp}h_{cfrp}}\right)\right] \quad (2)$$

2.5. Analysis of the fracture surfaces

Fracture surface images of the DCB samples were captured using a Keyence wide-area non-contact profilometer. Additionally, high-resolution, high-magnification images of selected regions of the fracture surfaces were obtained with a Bruker Scanning Electron Microscope (SEM).

3. Results

3.1. Surface morphology of the titanium adherends

Fig. 6 shows the surface topography of each type of sample, obtained as stitching of 4 scans for a total area of 2.83 × 2.83 mm^2. Table 3 shows the key surface morphological parameters: arithmetical mean height S_a, maximum height S_z, skewness S_{sk}, kurtosis S_{ku}, and peak density S_{pd} [40].

All samples exhibit positive skewness of the height profile ($S_{sk} > 0$), indicating the presence of high peaks across the surfaces. The kurtosis values (S_{ku}) are greater than 3, reflecting sharp peaks, particularly for the highest scan speeds and steep build angles. Notably, the sample 110–1250 demonstrates intermediate characteristics between the other 4 types of surface, with a S_a of 17.24 μm, almost perfectly corresponding to the average value across all 5 samples (average S_a = 17.13 μm).

3.2. Contact angle

The distilled water contact angle was evaluated between the intersection of the curve-fitted contour of the droplet and the surface of the sample (Fig. 7). The resulting contact angle was calculated as the average between the right and left ones.

Fig. 8 shows a bar graph with the contact angles for each batch of samples, with average values and standard deviation.

The samples printed vertically exhibit 6.8% lower contact angles, thus better wettability, compared with the samples printed at an angle (110-1250, 130-0500 and 130-2000).

The lower contact angle of the vertical samples is likely related to their lower surface roughness compared to the angle samples (−23%). This finding aligns with the previous work by the authors [36], where sandblasted samples showed lower surface roughness but higher wettability compared to the as-printed samples. Indeed, according to the wettability model developed by Cassie and Baxter [41], air pockets between the solid and the liquid phase prevent the drop to properly wet the surface, and an increase in roughness leads to an increase in number of air pockets. Thus, lower surface roughness promotes liquid spreading.

However, it should be noted that the contact angle measurements for both vertically and angled samples exhibit considerable variability (high standard deviations). This variability is likely due to the inherent heterogeneity of the surfaces, which affects droplet behavior and leads to inconsistencies in the measurements. Consequently, the data should be interpreted with caution, as the high variability may limit the robustness of the conclusions regarding the differences in wettability.

3.3. R-curves

Fig. 9 shows the average R-curves of the DCB samples. For each unloading segment, the average mode I fracture toughness and average crack length were calculated across the 3 repetitions for each batch. As shown in Fig. 9a, it is readily apparent that the samples printed with 90° build angle (hereafter "vertical" samples) have significantly higher steady state mode I fracture toughness compared to the samples printed at 110° and 130° (hereafter named "angle" samples).

Fig. 10 shows the normal plot of the effects highlighting the influence of the printing parameters on the steady-state G_{Ic}. The effects are calculated as half the difference between the average response at the high level and the average response at the low level of each factor. A positive effect indicates an increase in response (in this case, the steady-state G_{Ic}) and vice versa. The standardized effects, plotted on the X-axis, are dimensionless and allow for direct comparison across factors. The Y-axis represents the cumulative probability (percentile) of a normal distribution, helping to identify significant effects as those that deviate from the reference line. For further details on these calculations, the authors refer the reader to a textbook on the design of experiments ([42] among others). In this analysis, the level of significance (α) was set to 0.02, meaning that there is a 2% risk of identifying an effect as significant when it is actually due to random noise.

As shown in Fig. 10, the parameter build angle has a significantly higher standardized effect over the scan speed. Such effect is negative, meaning that increasing the build angle decreases the mode I fracture toughness. Additionally, the angle samples display a constant trend of G_{Ic} throughout the entire duration of the test, whereas the vertical samples display a rising R-curve trend, similar to that observed for several of the specimens analyzed in the previous work by the author [36]. Batch 90-2000 was the best performing overall, while batch 130-0500 exhibited the lowest G_{Ic}.

Table 4 shows the initial and steady-state G_{Ic}. The former was evaluated at the second unloading because, for several samples, the first unloading occurred during the linear-elastic phase of the test. The steady-state G_{Ic} was determined as the average of the second degree polynomial interpolation of the unloadings occurring from 85 mm to the end of the test for the vertical samples, and from 37 mm to 90 mm for the angle joints.

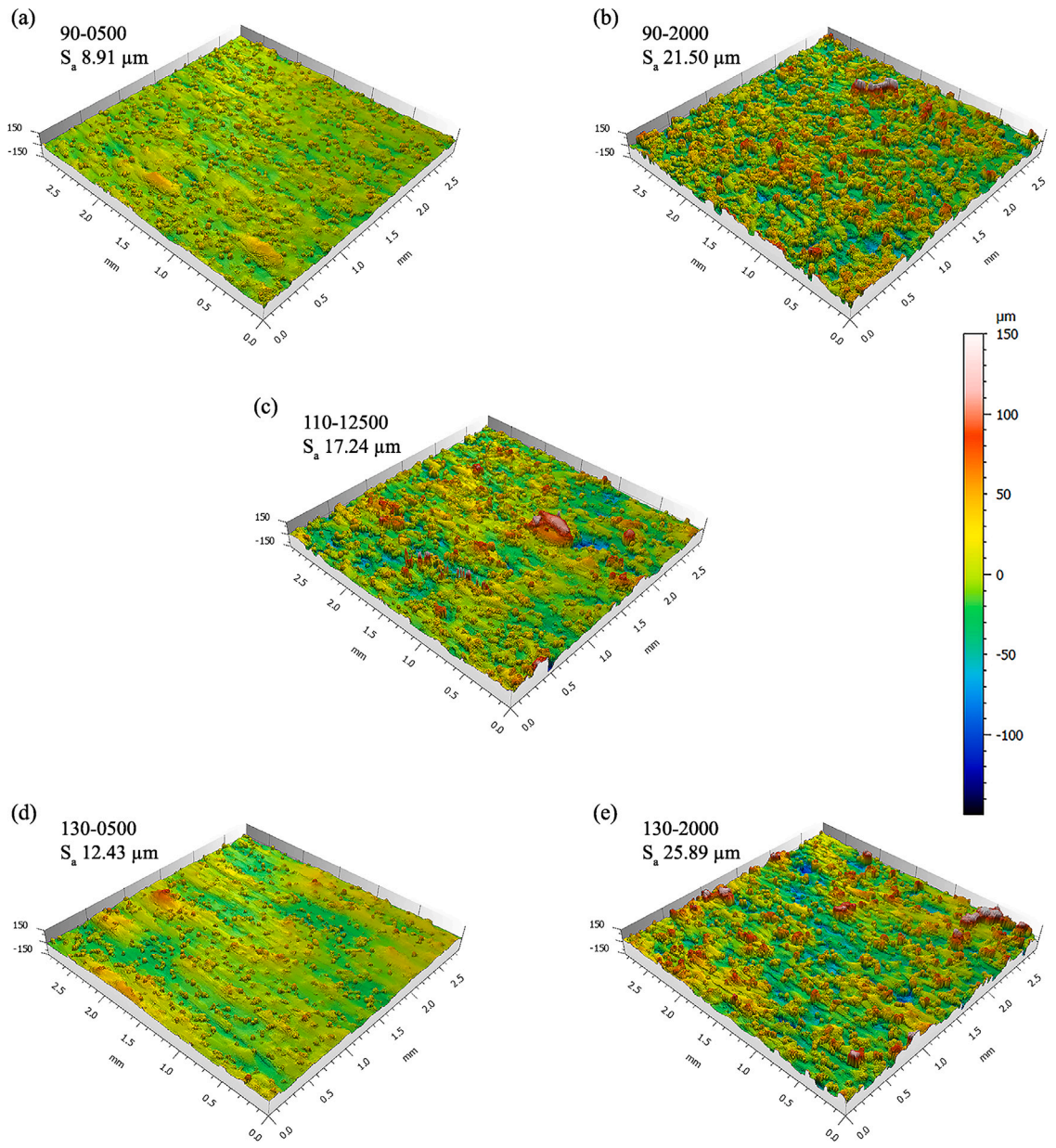

Fig. 6. Optical profilometry of the LPBF titanium surface.

Table 3
Surface parameters for the different batches.

	S_a [µm]	S_z [µm]	S_{sk} [–]	S_{ku} [–]	S_{pd} [1/mm^2]
90-0500	8.61 ± 0.37	93.24 ± 15.28	0.83 ± 0.13	4.31 ± 0.74	498.77 ± 62.57
90-2000	21.50 ± 1.72	203.56 ± 19.81	0.37 ± 0.12	2.98 ± 0.21	263.98 ± 48.00
110-1250	17.24 ± 1.87	190.11 ± 40.23	0.56 ± 0.32	4.17 ± 1.76	246.76 ± 60.91
130-0500	12.43 ± 1.38	114.69 ± 18.74	0.58 ± 0.24	3.88 ± 1.08	250.77 ± 71.18
130-2000	25.89 ± 2.89	294.00 ± 66.38	0.81 ± 0.33	4.83 ± 1.76	102.09 ± 37.82

3.4. Fracture surfaces of the DCB joints

The fracture surfaces of all the tested specimens are shown in Fig. 11. Notably, the vertical samples exhibit different failure modes compared to the angle samples. The former display mixed cohesive–adhesive failure in the first part of the crack propagation, with traces of adhesive on both the composite and the titanium substrates. In all the samples but sample 90-0500 1, the crack deflects between the first and the second ply of the CFRP adherend (Fig. 11).

4. Discussion

4.1. Surface morphology

4.1.1. Effect of scan speed at fixed build angle

Comparing samples fabricated at fixed build angle but varying scan speeds reveals a significant influence of the latter on the surface parameters S_a and S_z (e.g. batch 90-2000 + 150% increase in S_a against batch 90-0500).

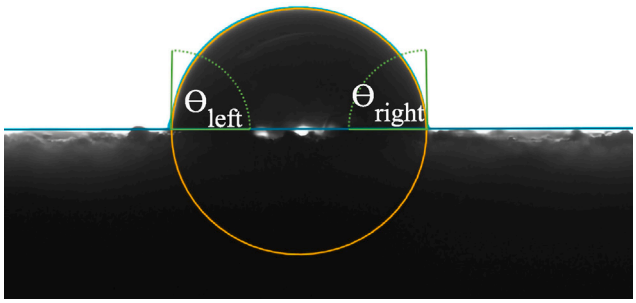

Fig. 7. Distilled water droplet, with curve-fitted contours for the calculation of the contact angles.

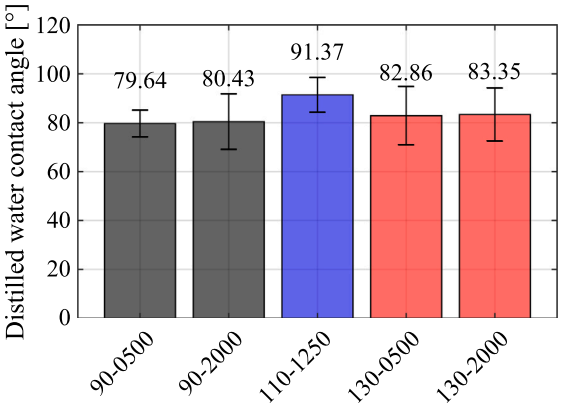

Fig. 8. Bar graph of the contact angles for each batch of samples.

Table 4
Summary of the results for the titanium-composite DCB joints.

	Initial G_{Ic}	Steady-state G_{Ic}
	[kJ/m^2]	
90-0500	0.41 ± 0.09	1.49 ± 0.05
90-2000	0.73 ± 0.19	1.64 ± 0.01
110-1250	0.36 ± 0.04	0.37 ± 0.00
130-0500	0.19 ± 0.03	0.22 ± 0.02
130-2000	0.47 ± 0.06	0.48 ± 0.02

Fig. 12 shows an enlarged portion of the profilometry for samples 90-0500 and 90-2000. The profilometry reveals that the former has a quite smooth core surface, with several small circular structures emerging from it. Such structures are titanium spherical particles which partially melted to the core surface during the manufacturing process. Indeed, the measured diameters of these structures are perfectly aligned with the average particle diameter of the Ti6Al4V powder (37.3 μm). In the surface of sample 90-2000, bigger structures were formed during the LPBF process, as demonstrated by the higher average equivalent diameter (see structure "D" in Fig. 12b). This phenomenon is known as "balling", and occurs when decreasing the input energy of the laser. It is worth noting that Pal et al. [43] also observed an increase of balling when increasing the laser scan speed for the manufacturing of LPBF Ti6Al4V samples. The height profile in Fig. 12a exhibits a relatively narrow range of variation, with peaks concentrated around 30 μm, which is close to the diameter of the Ti6Al4V powder particles. This distribution suggests a smoother surface morphology dominated by partially melted particles, with minimal evidence of balling. In contrast, the height distribution in Fig. 12b extends up to approximately 150 μm, displaying a broader and more irregular spread. Many peaks exceed 100 μm, indicating significant balling and material agglomeration due

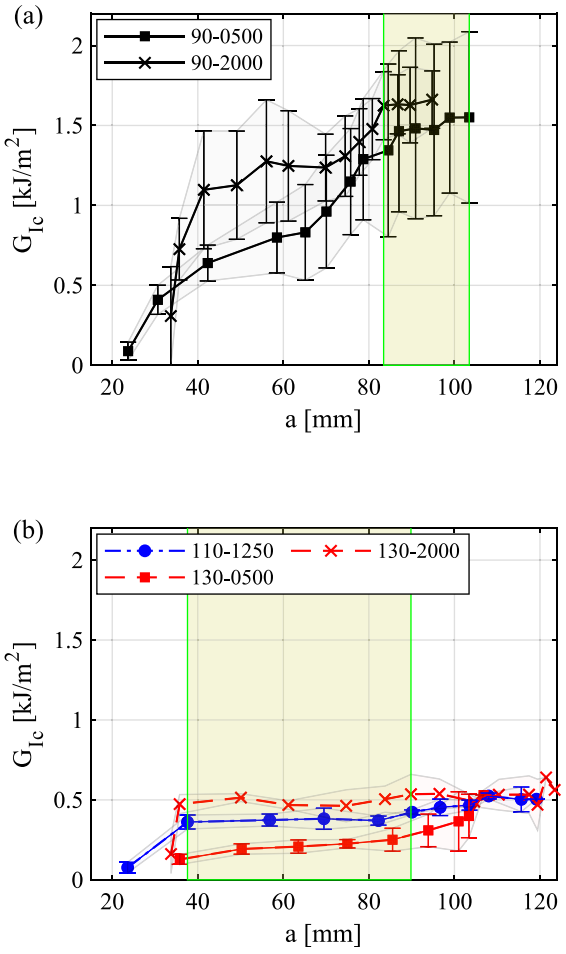

Fig. 9. R-curves. The steady-state propagation region is highlighted in translucent green.

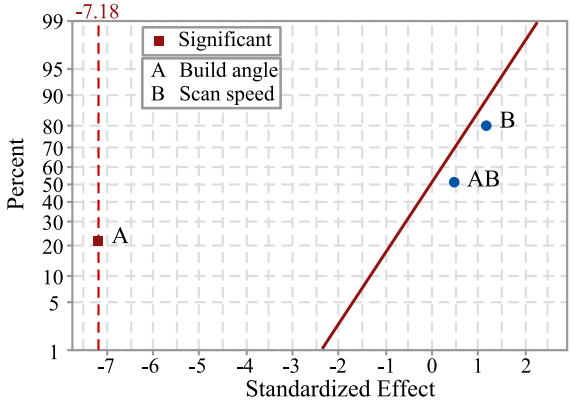

Fig. 10. Effect of the printing parameters on the steady-state fracture toughness.

to insufficient melting [43]. The wider and more scattered height distribution reflects the effects of the higher scan speed, which causes rapid cooling and destabilizes the melt pool.

This trend suggests that higher scan speeds reduce the energy input per unit area, resulting in incomplete melting and coalescence of powder particles into larger structures leading to rougher surfaces. This phenomenon is consistent across both build angles, and the same overall considerations can be made for samples 130-0500 and 130-2000, where the higher scan speed similarly results in a rougher

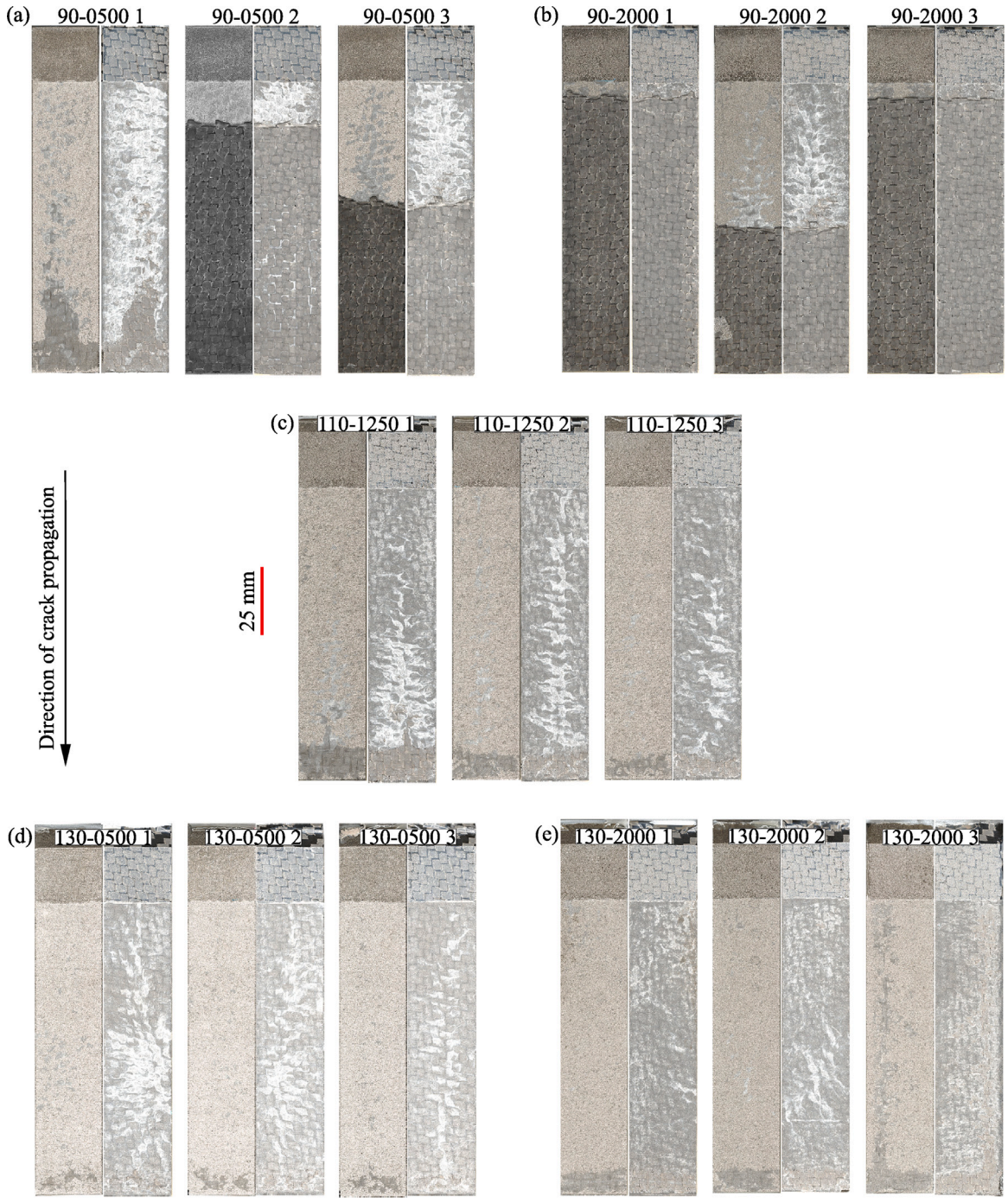

Fig. 11. Digital reconstruction of the fracture surfaces, acquired with a non-contact optical profilometer.

texture. However, these samples also exhibit parallel linear indentations attributed to the staircase effect, as discussed in the following section.

4.1.2. Effect of build angle at fixed scan speed

Comparing the surface of specimens 90-0500 (Fig. 6a) and 130-0500 (Fig. 6d), two main differences can be noted:

- Both specimens exhibit smooth core surfaces with partially melted particles, but sample 130-0500 features parallel linear indentations with regular spacing. These indentations, shown in Fig. 13, are layer lines visible in non-vertical prints, causing the "staircase effect" [44,45]. The staircase effect arises from the layer-by-layer nature of the LPBF process, where the resolution of each layer and the build angle determine the visibility and spacing of these marks. In fact, the distance between the parallel lines is in agreement with the layer height of 60 μm.
- The number of partially melted particles on the surface of samples 90-0500 is higher compared to the one of sample 130-0500. This is also confirmed by the two times higher surface peak density S_{pd}, which is the number of peaks per square millimeter.

The same overall considerations can be drawn also for samples 90-2000 and 130-2000, but with higher S_a and a more noticeable presence of the balling effect, as described in the previous section. In comparison with literature data, Ardila-Rodríguez [30] investigated Ti6Al4V-Ti6Al4V joints, and reported average surface roughness values

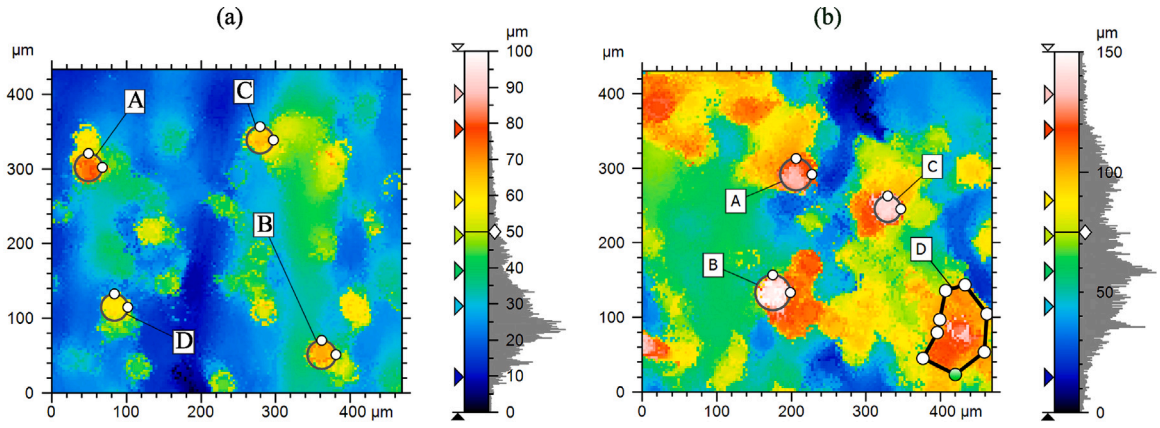

	Unit	A	B	C	D
Average height	µm	69.30	62.33	58.51	53.16
Equivalent diameter	µm	37.11	38.31	35.92	35.92

	Unit	A	B	C	D
Average height	µm	121.8	127.8	135.5	108.5
Equivalent diameter	µm	42.56	47.29	34.99	90.58

Fig. 12. Areas extracted from the samples (a) 90-0500 and (b) 90-2000.

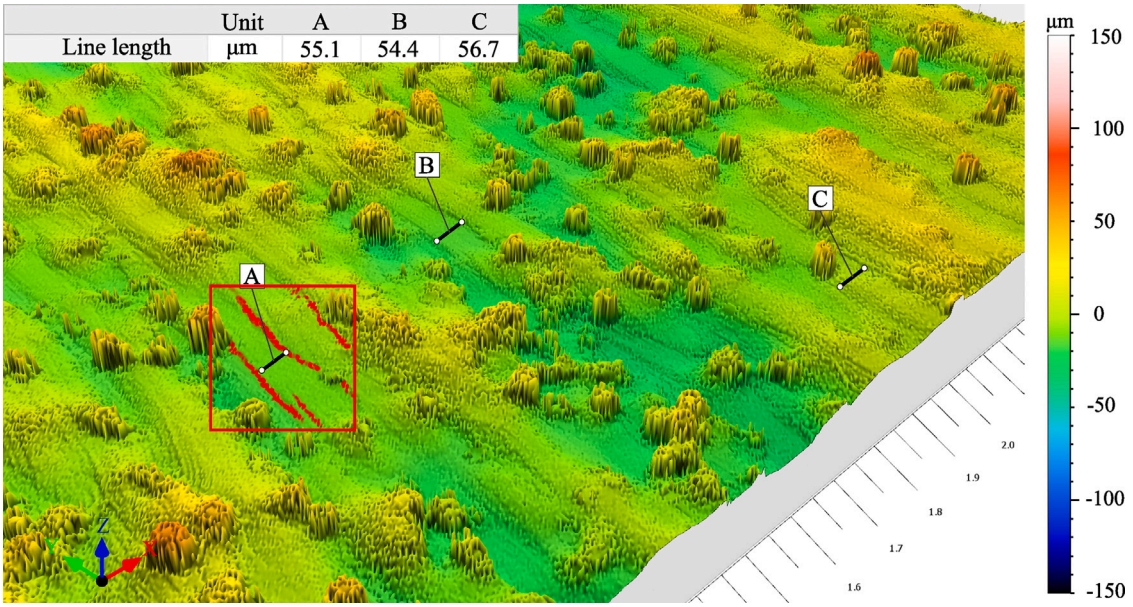

Fig. 13. Layer lines visible on the surface of sample 130-0500, with those around line "A" highlighted in red.

of 7.29 µm for vertically printed specimens and 10.85 µm for angled specimens. In our study, the corresponding values are higher, namely 15.05 µm for vertical specimens and 19.16 µm for specimens printed at a 40° angle; however, the overall trend is similar, with angled specimens exhibiting higher roughness. The observed differences could be attributed to the different combination of printing parameters, which were not fully specified in the mentioned study.

4.2. Fracture behavior of the samples and correlation with failure modes

The rising R-curve of the vertical joints up to the steady-state plateau (Fig. 9) is likely due to the competition between different failure modes. At crack initiation and in the first part of the propagation, the G_{Ic} is at its lowest values. The crack further propagates in the bondline and in the composite adherend at the same time (crack branching), as shown in Fig. 14a for joint 90-0500 2. In this stage, the fracture toughness increases with a steep trend from 1.47 kJ/m^2 to 1.95 kJ/m^2 when the crack deflects in the composite. After the crack deflection, a CFRP ligament is formed, bridging the composite and titanium adherends, thus further increasing the fracture toughness over 2 kJ/m^2 at the end of the test (Fig. 14b).

A similar trend was reported by Nguyen et al. [32] for LPBF Ti6Al4V–CFRP co-bonded DCB joints, namely an increase in fracture toughness with increasing crack length. Nguyen also reported crack deflection, consistent with the behavior observed in the present study. For a quantitative comparison, Nguyen et al. reported 1.1 kJ/m^2 of average fracture toughness in their study, comparable to the one measured in this work, namely 1.25 kJ/m^2 (evaluated excluding the first unloading, occurring in the linear-elastic phase of the test for several samples).

This behavior is absent in the angle joints, where the fracture surfaces predominantly reveal adhesive failure at the titanium–adhesive interface, as can be seen in Fig. 11c, d and e. Indeed, only a few traces of adhesive remain on the titanium adherends, which appear mostly clean. Instead, most of the adhesive residue is found on the composite substrates, indicating that the titanium–adhesive interface was the weakest link. The 90-2000 batch showed a similar behavior to the 90-0500 batch, with +10% higher values of steady-state G_{Ic}.

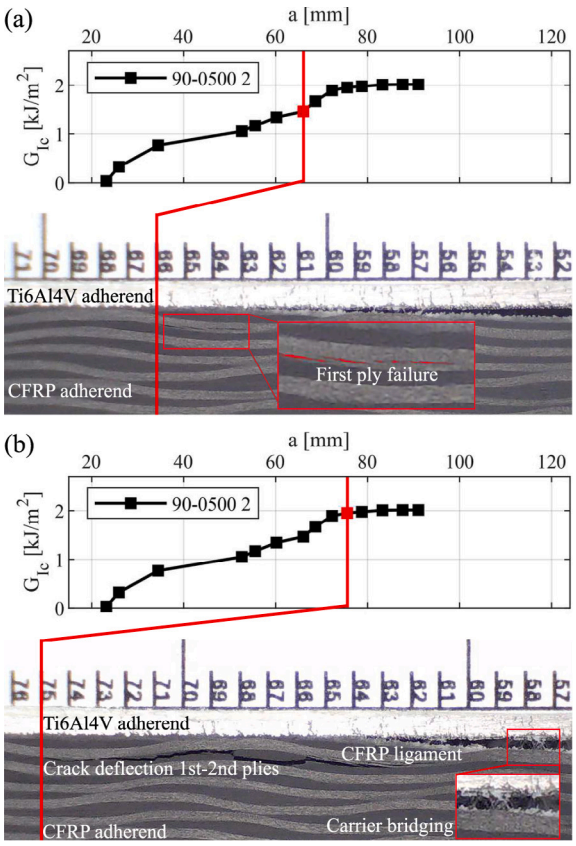

Fig. 14. Different failure modes for the vertical sample 90-0500 2.

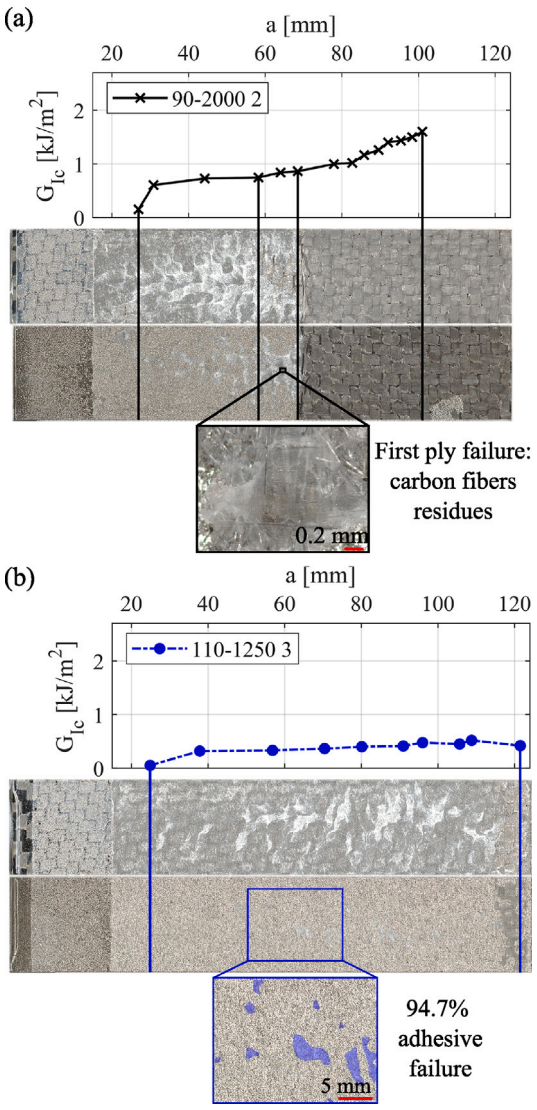

Fig. 15. Fracture surface against R-curve for sample (a) 90-2000 2 and sample 110-1250 3.

However, the standard deviations of the two batches overlap extensively, indicating that the difference in fracture toughness may not be statistically significant. The different behavior of the vertical and angle samples is also shown in Fig. 15, where the fracture surfaces of samples 90-2000 2 and 110-1250 3 are compared.

For sample 90-2000 2, three distinct regions of crack propagation can be identified. In the first area, ranging from approximately 25 to 60 mm, the failure mode is mainly adhesive, with little to no traces of adhesive on the titanium adherend. The fracture toughness is almost constant in this area, with an average value of 0.69 kJ/m^2. From 60 to 70 mm, an increase of adhesive on the titanium adherend can be seen. Moreover, the enlargement in Fig. 15a shows broken carbon fibers residues in the adhesive, indicating the initiation of first ply failure, associated with an increase in G_{Ic} up to 0.86 kJ/m^2. In the last part of the test, the crack propagates between the first and second ply of the CFRP adherend, with an increase in fracture toughness due to the branching of the crack and the formation of CFRP ligaments.

Sample 110-1250 3, on the other hand, displays adhesive failure throughout the entire crack propagation. This behavior reflects on its flat R-curve, with an average G_{Ic} of 0.41 kJ/m^2. A similar trend can be observed for all the angle samples, with the fracture surfaces mainly displaying adhesive failure. As shown in Table 4, the 130-0500 batch shows the lowest values of steady-state G_{Ic} (0.22 kJ/m^2). Among the angle samples, the batch 130-2000 exhibits the highest values of steady-state fracture toughness (0.48 kJ/m^2), followed by batch 110-1250 (0.37 kJ/m^2). Conversely, in the angle samples, the titanium–adhesive interface is weaker, resulting in adhesive failure as the sole failure mechanism. Crack deflection is therefore linked to adhesion strength: the earlier it occurs, the higher the fracture toughness. Most likely, in the vertical samples, the crack initiates at the titanium–adhesive interface, where it propagates until it reaches a region with high effective particle density. At this stage, the crack progressively moves towards the CFRP adherends.

This relationship is illustrated in Fig. 16, which presents the R-curves for each sample in batch 90-0500, including the only vertical sample that did not exhibit crack deflection — sample 90-0500 1 (Fig. 11). Notably, sample 90-0500 1 displayed the lowest fracture toughness, followed by sample 90-0500 3, where crack deflection occurred in the composite after 62 mm of propagation. Sample 90-0500 2 showed the highest fracture toughness among the batch, corresponding to crack deflection at the early stages of crack propagation (32 mm).

In order to isolate the toughening effect arising from delamination (multiple crack front and formation of CFRP ligaments), the mode I fracture toughness prior to crack deflection to the CFRP (hereafter referred to as “pre-delamination G_{Ic}”) was calculated for batch 90-0500 and batch 90-2000. Fig. 17 shows a bar graph with the pre-delamination G_{Ic}. Notably, the difference in pre-delamination fracture toughness between vertical and angle samples, while still significant (+50%), is less pronounced compared to the steady-state values. This highlights the difference between “global” fracture toughness, i.e. including the contribution of extrinsic energy dissipation phenomena

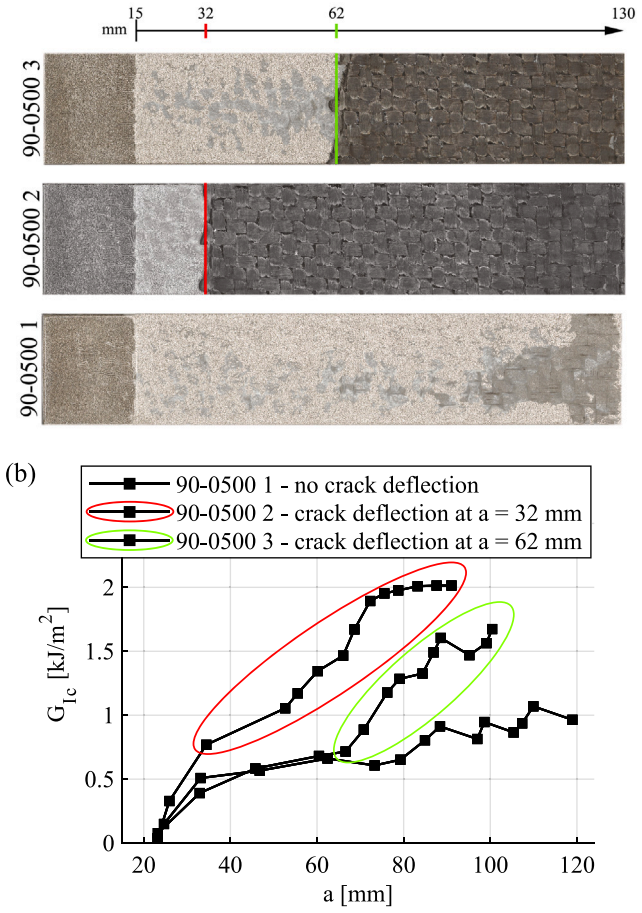

Fig. 16. (a) Fracture surfaces of the 90-0500 joints (only the titanium adherends) and (b) corresponding R-curves.

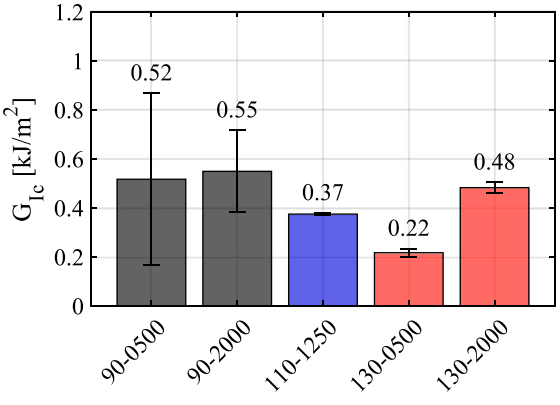

Fig. 17. Mode I fracture toughness before delamination for each batch.

(carrier bridging, first ply failure, delamination, CFRP ligament formation), and "local/effective" fracture toughness, attributable only to the adhesive and interfaces.

4.3. Effect of the surface morphology on the mode I fracture toughness

As demonstrated in the previous section, the results were polarized, with the vertical samples exhibiting significantly superior performance compared to the angle joints. This highlights the build angle as the most significant parameter influencing the fracture toughness under mode I loading. It is worth noting that at fixed build angles, the higher surface roughness left by the 2000 mm/s scan speed proved to be beneficial for the mode I fracture toughness. The 90-2000 and 130-2000 joints showed + 39% pre-delamination G_{Ic} over the counterparts printed at 500 mm/s.

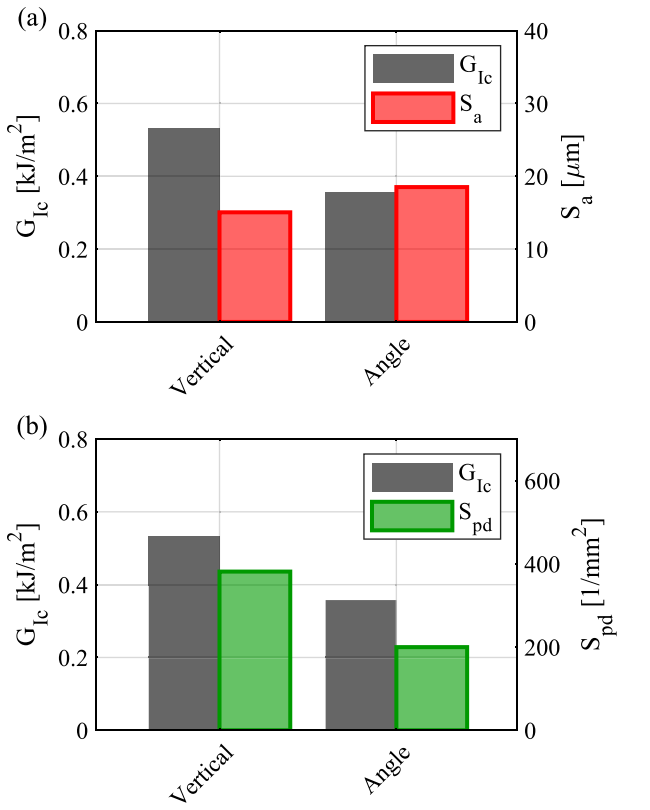

Fig. 18. Correlation between the pre-delamination mode I fracture toughness of vertical and angle samples and the surface parameters (a) S_a and (b) S_{pd}.

Nevertheless, the surface roughness was not directly correlated with the adhesion strength: comparing the samples printed with 90° and 130° the former presented 50% higher pre-delamination G_{Ic} over the latter in spite of the −21% lower S_a. As discussed in Section 4.1.2, the samples printed at 90° showed a surface with a higher number of partially melted particles compared to the angle samples (Fig. 6), as also proven by their higher S_{pd} (Table 3).

Fig. 18 shows the pre-delamination fracture toughness of the vertical and angle samples against their surface arithmetical mean height (Fig. 18a) and surface peak density (Fig. 18b). Interestingly, G_{Ic} shows a direct correlation with S_{pd}. This suggests that a higher number of partially melted powder particles improves adhesion strength. Likely, the undercuts between the partially melted powder particle and the core surface of the LPBF substrate promote mode I interlocking, which increases the adhesion strength of the as-printed titanium.

4.3.1. Scanning electron microscopy of the fracture surfaces

Fig. 19 shows the SEM images of the fracture surfaces of the joints, which clearly show that the partially melted titanium particles are almost perfectly spherical. This morphology leads to the formation of undercuts between the core titanium surface and the particles, in which the adhesive flows and then becomes mechanically interlocked during curing. The higher the number of partially melted particles, the greater the number of these undercuts, suggesting a direct correlation between the particle density (S_{pd}) and mode I fracture toughness. These observations align with the previously discussed optical profilometry results, further supporting the role of the number of partially melted particles on the mode I fracture behavior.

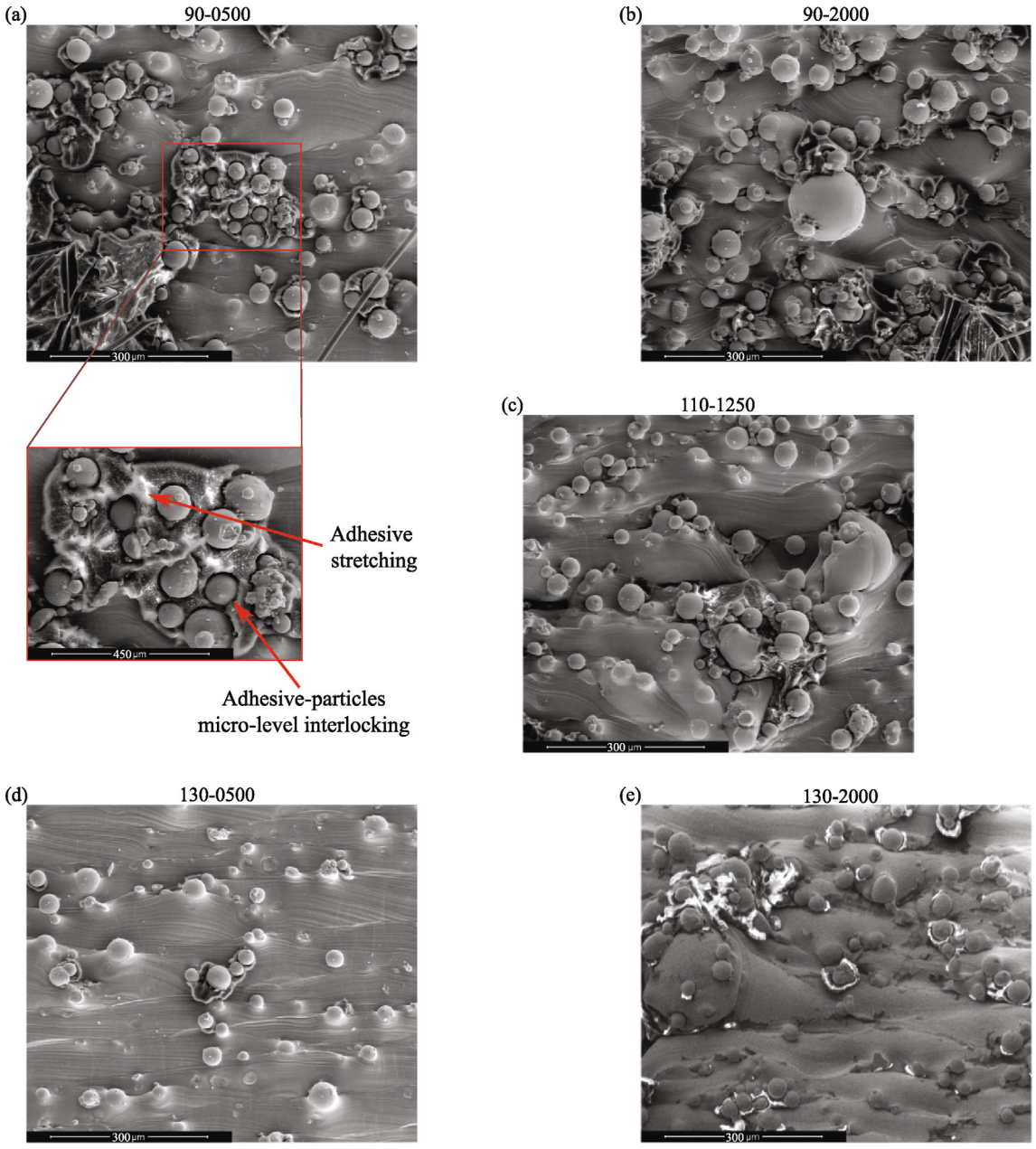

Fig. 19. Scanning electron micrograph of the fracture surfaces.

5. Estimation of the toughening effect of partially melted particles

The results of Section 4.3 show that the partially melted particles make a significant contribution to the adhesion strength of the LPBF surfaces. Although some studies have hinted at the beneficial role of partially melted particles [28,32], their effect has never been thoroughly investigated. In the following, a methodology is proposed to study this mechanism in detail.

5.1. Effective particle density

The first step in estimating the toughening role of the particles is to assess their surface density on the LPBF samples. In fact, while the S_{pd} is a viable parameter to predict the mode I adhesion strength of LPBF surfaces, it is only representative of the number of particles, since it considers every surface peak, regardless of its nature (layer lines, noise etc.).

Each surface height profile (three scans for each adherend — Section 2.2) was imported in Matlab, then centered on its mean plane. Contiguous points of the height profile above or below the mean plane were detected as blobs. The equivalent diameter of each blob above the mean plane — i.e. the diameter of a circle having the same area as the blob — was calculated from its area. Blobs whose diameters fell within the particle diameter range (20 to 63 µm, see Section 2.1) were counted as particles. However, some blobs exceeding this range contain individual particles that occupy only a portion of the blob area, leading to an underestimation of the total number of particles. To address this issue, discarded blobs were subjected to a second analysis, in which a local mean plane — one for each discarded blob, was recomputed and segmentation was reapplied above (or below) it, thereby isolating sub-blobs whose equivalent diameters fell within the valid range and recovering all particles in the final count (see Fig. 20). The number of particles was averaged within each batch, and the particle areal density was then calculated by dividing this average count by the scanned area (1.71×1.71 mm^2). Fig. 21a presents the

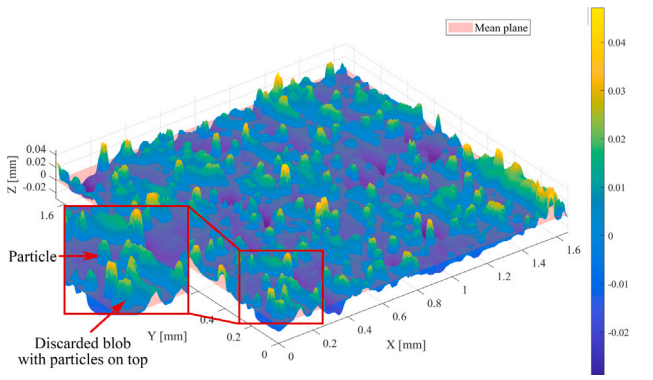

Fig. 20. Surface height profile.

effective particle density per batch, while Fig. 21b shows a scatter plot correlating the pre-delamination fracture toughness (Fig. 17) with the effective particle density. The plot indicates that higher particle areal densities correspond to increased mode I fracture toughness.

A rough estimate of the intrinsic interfacial fracture toughness of the LPBF surface, thus excluding the toughening contribution of partially melted particles, was obtained by linearly extrapolating the data in Fig. 21 to zero particle areal density. Ideally, this value should be determined on joints with particle-free adherends, but the LPBF process is not able to produce such surfaces. Another approach would be to polish the samples' surface, removing the particles. However, this option is not feasible as well, as polishing would remove the oxide layers on the LPBF surface, changing its chemistry. The extrapolated value is 0.06 kJ/m^2. Such value will be used for the development of FE models for the assessment of the particle toughening effect, as will be explained in the following section.

5.2. FE model of particle-adhesive unit cells

In order to quantitatively estimate the toughening effect of the partially melted particles, a FE model of Unit Cells (UC) containing a portion of the interface with a single partially melted particle was developed in Abaqus.

The UC was modeled with a two-dimensional plane-strain geometry (CPE4R elements), which is appropriate for representing a slice of the interface under mode-I loading. Although a fully three-dimensional representation of the particle geometry would be more realistic, such an extension would substantially increase the modeling complexity, and therefore lies beyond the scope of this work.

The height profile of single particles were taken from the fracture surface, together with the adhesive residues trapped beneath the undercuts. The height profiles were imported inside Abaqus, where the particles were assumed to be perfectly spherical (Fig. 22), as suggested from the findings of Section 4.3.1. The process was carried out on three different particle-adhesive height profiles (Fig. 22a and b), and their correspondent TSLs are shown in Fig. 22d — "particle 1 TSL", "particle 2 TSL" and "particle 3 TSL".

A Cohesive Zone Model (CZM) was used to capture the fracture behavior of unit cell, using bilinear Traction Separation Laws (TSLs) in the crack path taken from the optical profilometry. A TSL with the fracture toughness of the adhesive [35] was used were the crack propagated inside the adhesive, while the interfacial fracture toughness of 0.06 kJ/m^2 evaluated as in Section 5.1 was used in the particle-adhesive crack path. The CZM was implemented through a zero-thickness cohesive contact formulation. The parts in contact, namely the adhesive and the titanium adherend portion with the adhesive residues, were modeled with linear elastic material properties. Titanium properties from Table 2 were applied, while for the adhesive, the elastic modulus and Poisson's ratio were set to 3000 MPa and 0.4, respectively,

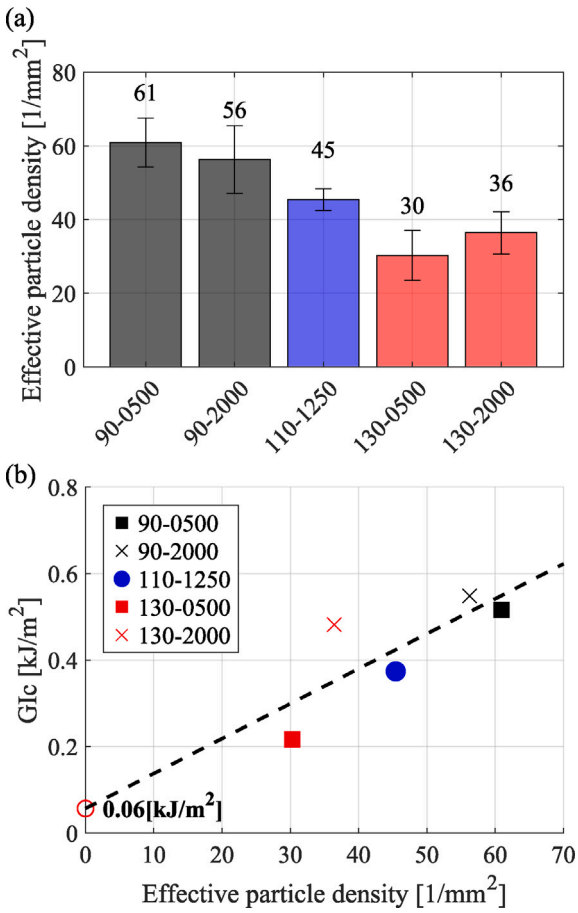

Fig. 21. (a) Bar graph of the effective particle density for each batch. Correlation between the effective particle density and the mode I fracture toughness before delamination.

which are typical for an epoxy [46]. To fully define the CZM, stiffness values of 1E6 N/mm^3 were assigned to each TSL. Such a high penalty stiffness is typically required in zero-thickness cohesive-contact formulations, as the elastic response of the interface should not contribute additional compliance, which is already captured by the surrounding material [47]. The values of maximum stress were set to 40 MPa for the adhesive (a reasonable value for a structural adhesive) and 9 MPa for the interfacial failure. The latter value, in the absence of experimental data, was selected so that the two triangular TSLs would share the same geometric proportions (i.e., identical initial stiffness and shape ratio between peak traction and corresponding separation). Since no experimental mode-II fracture data were available for the adhesive–substrate interface, the mode-I and mode-II TSLs were assumed to share the same shape and critical energy release rate. A mode I displacement was applied to the unit cell, and Periodic Boundary Conditions (PBCs) were applied to the left and right sides of the model. The reaction force and displacement in mode I were used to compute an equivalent homogenized traction separation law. The results are shown in Fig. 22, showing an increase of fracture toughness up to 15 times for the regions with particles when compared to the core surface. Indeed, the particle–core surface undercuts force the crack to propagate partly through the adhesive rather than entirely along the core surface (Fig. 22b, c). As a result, the fracture toughness of the UCs assumes an intermediate value between that of the core surface and that of the adhesive (0.89 kJ/m^2).

The proposed methodology represents an initial attempt to decouple the contributions of the core surface adhesion and particle interlocking to the fracture toughness of these joints. Future studies incorporating larger and more diverse datasets could further refine and validate this

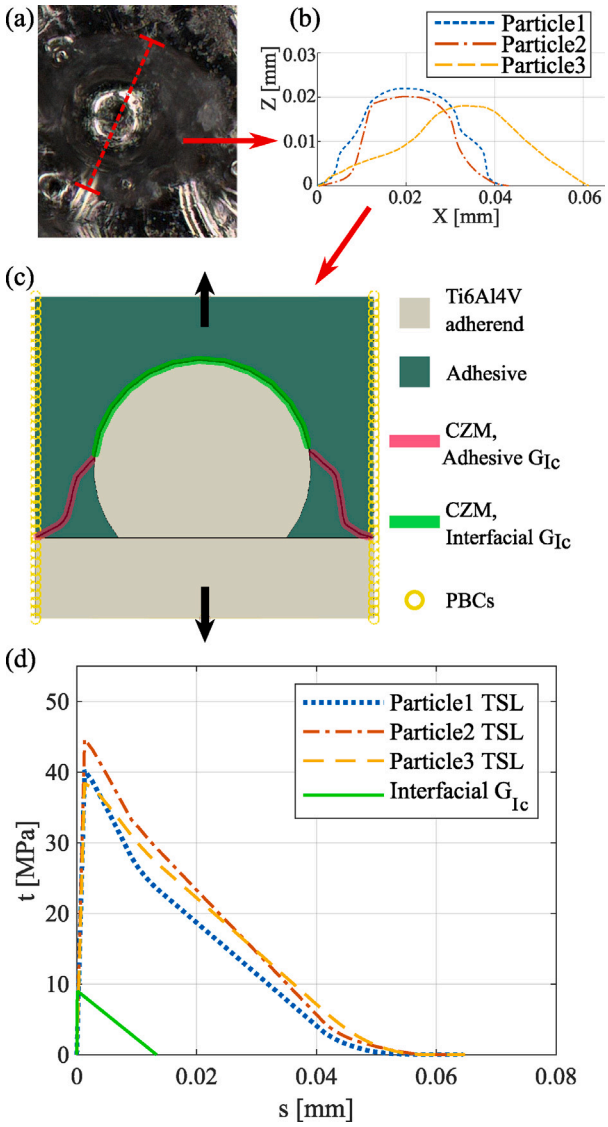

Fig. 22. From the height profile of a particle with adhesive residues (a,b), to the FE model of the particle-adhesive UC with Periodic Boundary Conditions (PBCs) (c) to the resulting homogenized TSLs (d).

approach. It should be emphasized that the present unit-cell model is not intended to reproduce the actual, non-periodic morphology of the interface, nor to provide a homogenized toughness of the entire joint. Instead, its scope is to isolate and quantify the local toughening contribution of an individual partially melted particle. To account for geometrical variability and provide statistical significance, three different particle–adhesive height profiles were extracted from the fracture surface and analyzed. The toughening effect reported here should therefore be interpreted as the average local effect of individual particles. A full representation of the fracture surface i.e. the homogenized toughness of the entire interface, lies beyond the scope of the present work. Nevertheless, the FE model confirms the toughening effect of partially melted particles, quantifies their contribution to the fracture toughness, and offers a mechanistic explanation for the observed correlation between particle density and adhesion strength.

6. Conclusions

In this work, the effect of different combinations of LPBF printing parameters has been evaluated on the mode I fracture toughness of titanium to CFRP co-bonded DCB joints. The joints were left as-printed i.e. no surface nor thermal treatment. Two printing parameters were chosen: the build angle, which was varied between 90° and 130° and the scan speed, varied between 500 mm/s and 2000 mm/s. A center point was also analyzed, with 110° build angle and 1250 mm/s scan speed.

The following conclusions can be drawn:

- The surface morphology of the titanium is strongly influenced by the laser scan speed. The samples printed with 2000 mm/s showed + 125% higher S_a compared to the samples printed at 500 mm/s. The build angle had a less significant effect on the roughness, with the samples printed at 130° showing + 27% higher S_a than the samples printed at 90°. The substrates printed at 110° and 1250 mm/s presented roughness nearly midway between those of the other samples.
- The surface of the samples printed at 90° presents a higher number of partially melted powder particles, as demonstrated by the + 91% higher surface peak density S_{pd} and 58% higher effective particle density compared to the samples printed at 110° and 130°.
- No major differences in wettability were observed among the batches of samples: the ones printed at lower build angle exhibited slightly lower distilled water contact angles (−7%) compared to the ones printed at 130°. These findings are in accordance to the model of Cassie–Baxter [41], according to which liquids tend to not wet deep valleys in solid surfaces (high roughness surfaces).
- Samples printed at 90° exhibit a steady-state mode I fracture toughness 3.4 times higher than those printed at 110° and 130°, despite having 21% lower roughness. The scan speed had a less significant effect on the adhesion strength, with the samples printed at 2000 mm/s exhibiting + 24% G_{Ic} compared to those printed at 500 mm/s. This trend is attributed to the higher number of partially melted particles on the surface of the vertically printed samples. As demonstrated by a novel methodology involving FE analysis, the particles enhance interfacial interlocking and thus adhesion strength. However, it should be noted that the FE model relies on a simplified 2D homogenized unit-cell representation, which does not fully capture the non-periodic and inherently three-dimensional nature of the as-printed surfaces. These modeling simplifications should be considered when interpreting the quantitative outcomes of the FE analysis.

As a general conclusion, the surface roughness seems not to be the only quantitative parameter associated with adhesion strength. The "quality" of the surface also has to be studied, as different types of morphologies can promote interlocking only triggered under a specific loading mode. For the Ti6Al4V–CFRP co-bonded joints examined in this work, the optimal parameters combination would be 90° print angle and 2000 mm/s scan speed.

These findings provide new insight for the design of reliable, high-performance bonded structures using as-printed components and open new perspectives for tuning LPBF parameters to maximize interfacial adhesion.

CRediT authorship contribution statement

Michele Gulino: Writing – original draft, Methodology, Investigation, Formal analysis, Conceptualization. **Rosemere de Araujo Alves Lima:** Writing – review & editing, Methodology, Investigation, Formal analysis, Conceptualization. **Fabrizio Moroni:** Writing – review & editing, Supervision, Project administration, Conceptualization. **Francesco Musiari:** Writing – review & editing, Investigation, Formal analysis. **Alessandro Pirondi:** Writing – review & editing, Supervision, Project administration, Conceptualization. **Sofia Teixeira de Freitas:** Writing – review & editing, Supervision, Project administration, Conceptualization.

Declaration of competing interest

The authors declare that they have no known competing financial interests or personal relationships that could have appeared to influence the work reported in this paper.

Acknowledgments

This research was carried out within the framework of the project DOT13SJY60, Ministerial Decree No. 1061 of 10/08/2021, and was funded under the "Programma Operativo Nazionale" (PON), Action IV.4 "PhD grant on Innovation Thematics", Portugal. The authors acknowledge Fundação para a Ciência e a Tecnologia (FCT), Portugal for its financial support via the project LAETA Base Funding (10.54499/UIDB/50022/2020). Valuable support was provided by Bercella Srl and 3T-Additive Manufacturing, Portugal, who provided the materials used in this study. The authors also thank Peter Jerrard and Matteo Menoni for their guidance throughout the experimental campaign and the development of this work.

Appendix. Preliminary DoE

A preliminary build with small rectangular cross section prints ($10 \times 10 \times 3$ mm^3) was carried to study the effect of the variation of printing parameters on their surface morphology. Three printing parameters were varied, each on two levels (3^2 factorial design):

- Build angle, 90° and 135° defined as the angle formed between the upface and the build platform (see Fig. A.1)
- Laser scan speed, 500 mm/s and 2000 mm/s
- Laser Power, 100 W and 300 W

The experiment matrix and the geometry of the prints are shown in Table A.1 and Fig. A.1, respectively.

Table A.1
Design of experiment for the preliminary build, with a total of 8 design points.

	Low level (–)	High level (+)	
Build angle (a) [°]	90	135	
Laser scan speed (b) [mm/s]	500	2000	
Laser power (c) [W]	100	300	
Design point	Parameter (a)	Parameter (b)	Parameter (c)
(1)	–	–	–
A	+	–	–
B	–	+	–
C	–	–	+
AB	+	+	–
AC	+	–	+
BC	–	+	+
ABC	+	+	+

Three repetitions were printed for each design point, for a total of 24 specimens. The surface morphology of each the preliminary prints was inspected with a Taylor-Hobson optical profilometer, scanning three 1.71×1.71 mm^2 square areas per sample. The areas were scanned on the lateral face of the vertically printed samples and on the upface of those printed with a 135° build angle.

The resulting surface arithmetical mean area S_a is shown in Table A.2, with the average values and the standard deviation for each batch.

Upon initial observation of the surface parameters, it is evident that the range of attainable roughness is wide, spanning from 10.99 μm to 29.87 μm (+ 172%). ANalysis Of VAriance (ANOVA) was carried out to determine which are the most influential printing parameters. The normal plot of effects, shown in Fig. A.2 highlights the influence of printing parameters on the surface roughness.

Among the analyzed factors, the build angle A emerges as the most significant parameter, as it deviates markedly from the reference line,

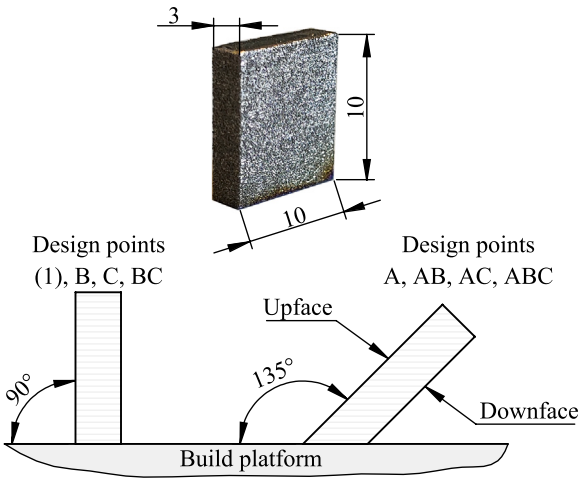

Fig. A.1. Geometry and dimensions (in millimeters) of the preliminary prints.

Table A.2
S_a for each batch of the preliminary build.

	Build angle [°]	Scan speed [mm/s]	Laser power [W]	S_a [μm]
(1)	90	500	100	20.63 ± 1.65
A	135	500	100	23.47 ± 0.93
B	90	2000	100	17.60 ± 0.93
C	90	500	300	10.99 ± 0.87
AB	135	2000	100	27.50 ± 5.26
AC	135	500	300	17.17 ± 2.58
BC	90	2000	300	14.40 ± 0.85
ABC	135	2000	300	29.87 ± 2.82

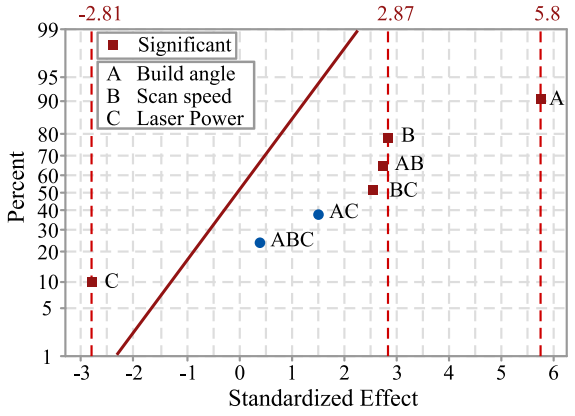

Fig. A.2. Normal plot of the effect of printing parameters and their combinations on the surface arithmetical mean height S_a.

indicating a substantial impact on the response. Scan speed is the second most influential parameter affecting roughness, closely followed by laser power. However, while scan speed has a positive effect on roughness, laser power exhibits a negative impact. The two and three-way interactions, especially BC, AC and ABC, exhibit less pronounced effects.

Due to the high cost of the prints, the number of builds for the final DCB samples had to be reduced. Thus, the parameters of choice were the build angle and the laser scan speed, which had the highest effects.

Data availability

Data will be made available on request.

References

[1] L. da Silva, A. Öchsner, R. Adams, Handbook of Adhesion Technology, Springer Berlin Heidelberg, 2011, http://dx.doi.org/10.1007/978-3-642-01169-6.

[2] D.A. Dillard, Advances in Structural Adhesive Bonding, vol. 18, Pergamon, 2011, p. 530, http://dx.doi.org/10.1533/9781845698058.

[3] P.P. Camanho, F.L. Matthews, Stress analysis and strength prediction of mechanically fastened joints in FRP: a review, Compos. A 28 (1997) 529–547, http://dx.doi.org/10.1016/S1359-835X(97)00004-3.

[4] C. Ashforth, L. Ilcewicz, Certification of bonded aircraft structure and repairs.

[5] T.A.S. Fuertes, T. Kruse, T. Körwien, M. Geistbeck, Bonding of CFRP primary aerospace structures - Discussion of the certification boundary conditions and related technology fields addressing the needs for development, Compos. Interfaces 22 (2015) 795–808, http://dx.doi.org/10.1080/09276440.2015.1077048.

[6] N. Razavi, E. Esmaeili, M. Samari, S. Razavi, Stress analysis on a non-flat zigzag interface bonded joint, J. Adhes. 94 (2018) 199–217, http://dx.doi.org/10.1080/00218464.2016.1257942.

[7] F. Musiari, F. Moroni, A.H.A. Lutey, Enhanced mechanical interlocking of adhesive-bonded joints via tailored serrated patterns manufactured with laser ablation, J. Adhes. 101 (2023) 56–90, http://dx.doi.org/10.1080/00218464.2023.2285431.

[8] K. Maloney, N. Fleck, Toughening strategies in adhesive joints, Int. J. Solids Struct. 158 (2019) 66–75, http://dx.doi.org/10.1016/j.ijsolstr.2018.08.028.

[9] S. Heide-Jørgensen, S.T. de Freitas, M.K. Budzik, On the fracture behaviour of CFRP bonded joints under mode I loading: Effect of supporting carrier and interface contamination, Compos. Sci. Technol. 160 (2018) 97–110, http://dx.doi.org/10.1016/j.compscitech.2018.03.024.

[10] F. Smith, COMELD™: An innovation in composite to metal joining, Mater. Technol. 20 (2005) 91–96, http://dx.doi.org/10.1080/10667857.2005.11753117.

[11] A.P. Mouritz, Review of z-pinned composite laminates, 2007, pp. 2383–2397, http://dx.doi.org/10.1016/j.compositesa.2007.08.016.

[12] S. Ucsnik, M. Scheerer, S. Zaremba, D.H. Pahr, Experimental investigation of a novel hybrid metal-composite joining technology, Compos. A: Appl. Sci. Manuf. 41 (2010) 369–374, http://dx.doi.org/10.1016/j.compositesa.2009.11.003.

[13] P.N. Parkes, R. Butler, J. Meyer, A. de Oliveira, Static strength of metal-composite joints with penetrative reinforcement, Compos. Struct. 118 (2014) 250–256, http://dx.doi.org/10.1016/j.compstruct.2014.07.019.

[14] L. Raimondi, L. Tomesani, A. Zucchelli, Enhancing the robustness of hybrid metal-composite connections through 3D printed micro penetrative anchors, Appl. Compos. Mater. 31 (2024) 1275–1293, http://dx.doi.org/10.1007/s10443-024-10224-1.

[15] L. Raimondi, L. Tomesani, L. Donati, A. Zucchelli, Lattice material infiltration for hybrid metal-composite joints: Manufacturing and static strenght, Compos. Struct. 269 (2021) http://dx.doi.org/10.1016/j.compstruct.2021.114069.

[16] T. Bagnato, A.R. Ravindran, A. Mirabedini, R.B. Ladani, E. Kandare, A.C. Orifici, P. Chang, J. Wang, A.P. Mouritz, Superior interfacial toughening of hybrid metal-composite structural joints using 3D printed pins, Compos. A: Appl. Sci. Manuf. 168 (2023) http://dx.doi.org/10.1016/j.compositesa.2023.107479.

[17] J.F. Durodola, Functionally graded adhesive joints – A review and prospects, Int. J. Adhes. Adhes. 76 (2017) 83–89, http://dx.doi.org/10.1016/j.ijadhadh.2017.02.008.

[18] G.A. Wade, W.J. Cantwell, Adhesive bonding and wettability of plasma treated, glass fiber-reinforced nylon-6,6 composites, J. Mater. Sci. Lett. 19 (2000) 1829–1832, http://dx.doi.org/10.1023/A:1006706826209.

[19] F. Moroni, F. Musiari, C. Favi, Effect of the surface morphology over the fatigue performance of metallic single lap-shear joints, Int. J. Adhes. Adhes. 97 (2020) http://dx.doi.org/10.1016/j.ijadhadh.2019.102484.

[20] A. Safari, M. Farahani, P. Ghabezi, Experimental study on the influences of different surface treatment processes and adhesive type on the aluminum adhesive-bonded joint strength, Mech. Des. Struct. Mach. 50 (2022) 2400–2413, http://dx.doi.org/10.1080/15397734.2020.1777876.

[21] A.J. Kinloch, Adhesion and Adhesives, Springer Netherlands, 1987, http://dx.doi.org/10.1007/978-94-015-7764-9.

[22] G. Strano, L. Hao, R.M. Everson, K.E. Evans, Surface roughness analysis, modelling and prediction in selective laser melting, J. Mater. Process. Technol. 213 (2013) 589–597, http://dx.doi.org/10.1016/j.jmatprotec.2012.11.011.

[23] A.M. Khorasani, I. G., A.R. Ghaderi, Rheological characterization of process parameters influence on surface quality of Ti-6Al-4V parts manufactured by selective laser melting, Int. J. Adv. Manuf. Technol. 97 (2018) 3761–3775, http://dx.doi.org/10.1007/s00170-018-2168-6.

[24] W. Cai, Q. Song, H. Ji, M.K. Gupta, Multi-perspective analysis of building orientation effects on microstructure, mechanical and surface properties of slm ti6al4v with specific geometry, Materials 14 (2021) http://dx.doi.org/10.3390/ma14164392.

[25] M. Ahmed, M.A. Obeidi, S. Yin, R. Lupoi, Influence of processing parameters on density, surface morphologies and hardness of as-built Ti-5Al-5Mo-5V-3Cr alloy manufactured by selective laser melting, J. Alloys Compd. 910 (2022) http://dx.doi.org/10.1016/j.jallcom.2022.164760.

[26] T. Maconachie, M. Leary, B. Lozanovski, X. Zhang, M. Qian, O. Faruque, M. Brandt, SLM lattice structures: Properties, performance, applications and challenges, 2019, http://dx.doi.org/10.1016/j.matdes.2019.108137.

[27] M. Grasso, B.M. Colosimo, Process defects and in situ monitoring methods in metal powder bed fusion: a review, Meas. Sci. Technol. 28 (2017) 044005, http://dx.doi.org/10.1088/1361-6501/aa5c4f.

[28] E. Ertürk, B. Musil, G. Diez, C. Felber, P. Höfer, Surface morphology influences of PBF-LB manufactured Ti6Al4V parts on adhesive bond strength—investigation of as-built and surface-treated conditions, Prog. Addit. Manuf. 8 (2023) 719–731, http://dx.doi.org/10.1007/s40964-023-00450-7.

[29] C. Koch, J. Richter, M. Vollmer, M. Kahlmeyer, T. Niendorf, S. Böhm, Adhesively bonded joints in components manufactured via selective laser melting, Proc. Inst. Mech. Eng. C: J. Mech. Eng. Sci. 235 (2021) 518–526, http://dx.doi.org/10.1177/0954406220959376.

[30] L. Ardila-Rodríguez, C. Rans, J. Poulis, Effect of surface morphology on the Ti–Ti adhesive bond performance of Ti6Al4V parts fabricated by selective laser melting, Int. J. Adhes. Adhes. 110 (2021) http://dx.doi.org/10.1016/j.ijadhadh.2021.102918.

[31] N. Naat, Y. Boutar, S. Naïmi, S. Mezlini, L.F. da Silva, A.H. Bashiri, Influence of bio-inspired surface texture of additively manufactured 17-4 PH stainless steel adherends on the strength of adhesively bonded joints, Int. J. Adhes. Adhes. 126 (2023) http://dx.doi.org/10.1016/j.ijadhadh.2023.103478.

[32] A.T. Nguyen, M. Brandt, A.C. Orifici, S. Feih, Hierarchical surface features for improved bonding and fracture toughness of metal-metal and metal-composite bonded joints, Int. J. Adhes. Adhes. 66 (2016) 81–92, http://dx.doi.org/10.1016/j.ijadhadh.2015.12.005.

[33] Z. Fielden-Stewart, T. Coope, D. Bacheva, B.C. Kim, Effect of the surface morphology of SLM printed aluminium on the interfacial fracture toughness of metal-composite hybrid joints, Int. J. Adhes. Adhes. 105 (2021) http://dx.doi.org/10.1016/j.ijadhadh.2020.102779.

[34] F. Moroni, A. Pirondi, C. Pernechele, L. Vescovi, Comparison of tensile strength and fracture toughness of Co-Bonded and Cold-Bonded carbon fiber Laminate-Aluminum adhesive joints, Materials (2021) http://dx.doi.org/10.3390/ma14143778.

[35] M. Gulino, F. Moroni, A. Pirondi, Metal-metal and metal-composite joints with 3D printed aluminium substrates: effect of surface treatment on the mode I fracture toughness, J. Adhes. (2023) http://dx.doi.org/10.1080/00218464.2023.2285074.

[36] M. Gulino, R.A.A. Lima, F. M., A. P., S.T. de Freitas, Effect of the surface morphology of 3D printed titanium substrates on the mode I fracture toughness of metal-metal and metal-composite bonded joints, Theor. Appl. Fract. Mech. 135 (2025) 104778, http://dx.doi.org/10.1016/j.tafmec.2024.104778.

[37] X. Wang, J. Ahn, Q. Bai, W. Lu, J. Lin, Effect of forming parameters on electron beam Surfi-Sculpt protrusion for Ti-6Al-4V, Mater. Des. 76 (2015) 202–206, http://dx.doi.org/10.1016/j.matdes.2015.03.065.

[38] A. International, Standard test method for fracture strength in cleavage of adhesives in bonded metal joints, 2020.

[39] M.F. de Moura, R.D. Campilho, J.P. Gonçalves, Crack equivalent concept applied to the fracture characterization of bonded joints under pure mode I loading, Compos. Sci. Technol. 68 (2008) 2224–2230, http://dx.doi.org/10.1016/j.compscitech.2008.04.003.

[40] I.O. for Standardization, Geometrical product specifications (GPS)-Surface texture: Areal-Part 2, 2021.

[41] A.B. Cassie, S. Baxter, Wettability of porous surfaces, Trans. Faraday Soc. 40 (1944) 546–551, http://dx.doi.org/10.1039/tf9444000546.

[42] D.C. Montgomery, Design and Analysis of Experiments, John Wiley & Sons, Inc., 2017.

[43] S. Pal, G. Lojen, R. Hudak, V. Rajtukova, T. Brajlih, V. Kokol, I. Drstvenšek, As-fabricated surface morphologies of Ti-6Al-4V samples fabricated by different laser processing parameters in selective laser melting, Addit. Manuf. 33 (2020) http://dx.doi.org/10.1016/j.addma.2020.101147.

[44] S. Pereira, A.I. Vaz, L.N. Vicente, On the optimal object orientation in additive manufacturing, Int. J. Adv. Manuf. Technol. 98 (2018) 1685–1694, http://dx.doi.org/10.1007/s00170-018-2218-0.

[45] F. Cabanettes, A. Joubert, G. Chardon, V. Dumas, J. Rech, C. Grosjean, Z. Dimkovski, Topography of as built surfaces generated in metal additive manufacturing: A multi scale analysis from form to roughness, Precis. Eng. 52 (2018) 249–265, http://dx.doi.org/10.1016/j.precisioneng.2018.01.002.

[46] I.S. Abbood, S.A. Odaa, K.F. Hasan, M.A. Jasim, Properties evaluation of fiber reinforced polymers and their constituent materials used in structures - A review, in: Materials Today: Proceedings, Vol. 43, Elsevier Ltd, 2021, pp. 1003–1008, http://dx.doi.org/10.1016/j.matpr.2020.07.636.

[47] P.P. Camanho, C.G. Dávila, M.F.D. Moura, Numerical simulation of mixed-mode progressive delamination in composite materials, J. Compos. Mater. 37 (2003) 1415–1438, http://dx.doi.org/10.1177/0021998303034505.